Hyperspectral imaging for label-free in vivo identification of myocardial scars and sites of radiofrequency ablation lesions ℮

Luther M. Swift, PhD,* Huda Asfour, PhD,* Narine Muselimyan, MD,*
Cinnamon Larson, PhD,† Kenneth Armstrong, MSc,† Narine A. Sarvazyan, PhD*

*From the *The George Washington University School of Medicine and Health Sciences, Washington, District of Columbia, and †Nocturnal Product Development, Durham, North Carolina.*

BACKGROUND Treatment of cardiac arrhythmias often involves ablating viable muscle tissue within or near islands of scarred myocardium. Yet, today there are limited means by which the boundaries of such scars can be visualized during surgery and distinguished from the sites of acute injury caused by radiofrequency (RF) ablation.

OBJECTIVE We sought to explore a hyperspectral imaging (HSI) methodology to delineate and distinguish scar tissue from tissue injury caused by RF ablation.

METHODS RF ablation of the ventricular surface of live rats that underwent thoracotomy was followed by a 2-month animal recovery period. During a second surgery, new RF lesions were placed next to the scarred tissue from the previous ablation procedure. The myocardial infarction model was used as an alternative way to create scar tissue.

RESULTS Excitation-emission matrices acquired from the sites of RF lesions, scar region, and the surrounding unablated tissue re-

vealed multiple spectral changes. These findings justified HSI of the heart surface using illumination with 365 nm UV light while acquiring spectral images within the visible range. Autofluorescence-based HSI enabled to distinguish sites of RF lesions from scar or unablated myocardium in open-chest rats. A pilot version of a percutaneous HSI catheter was used to demonstrate the feasibility of RF lesion visualization in atrial tissue of live pigs.

CONCLUSION HSI based on changes in tissue autofluorescence is a highly effective tool for revealing—in vivo and with high spatial resolution—surface boundaries of myocardial scar and discriminating it from areas of acute necrosis caused by RF ablation.

KEYWORDS Ablation; Hyperspectral imaging; Myocardium; Scar

(Heart Rhythm 2018;15:564–575) © 2017 The Authors. Published by Elsevier Inc. on behalf of Heart Rhythm Society. This is an open access article under the CC BY-NC-ND license (http://creativecommons.org/licenses/by-nc-nd/4.0/).

Introduction

To eliminate arrhythmogenic activity associated with scars, new rounds of tissue ablation often need to be performed. To achieve a more precise targeting of arrhythmogenic sources and pathways, it can be extremely helpful to visualize scar boundaries and any isthmuses of viable tissue within the scar while doing the next round of ablation procedures. A number of approaches are currently being developed to address this need, including several noninvasive techniques that help identify scar transmurality.[1,2] Yet, as of today, these approaches require additional surgery time and the injection of contrast agents and offer a relatively low
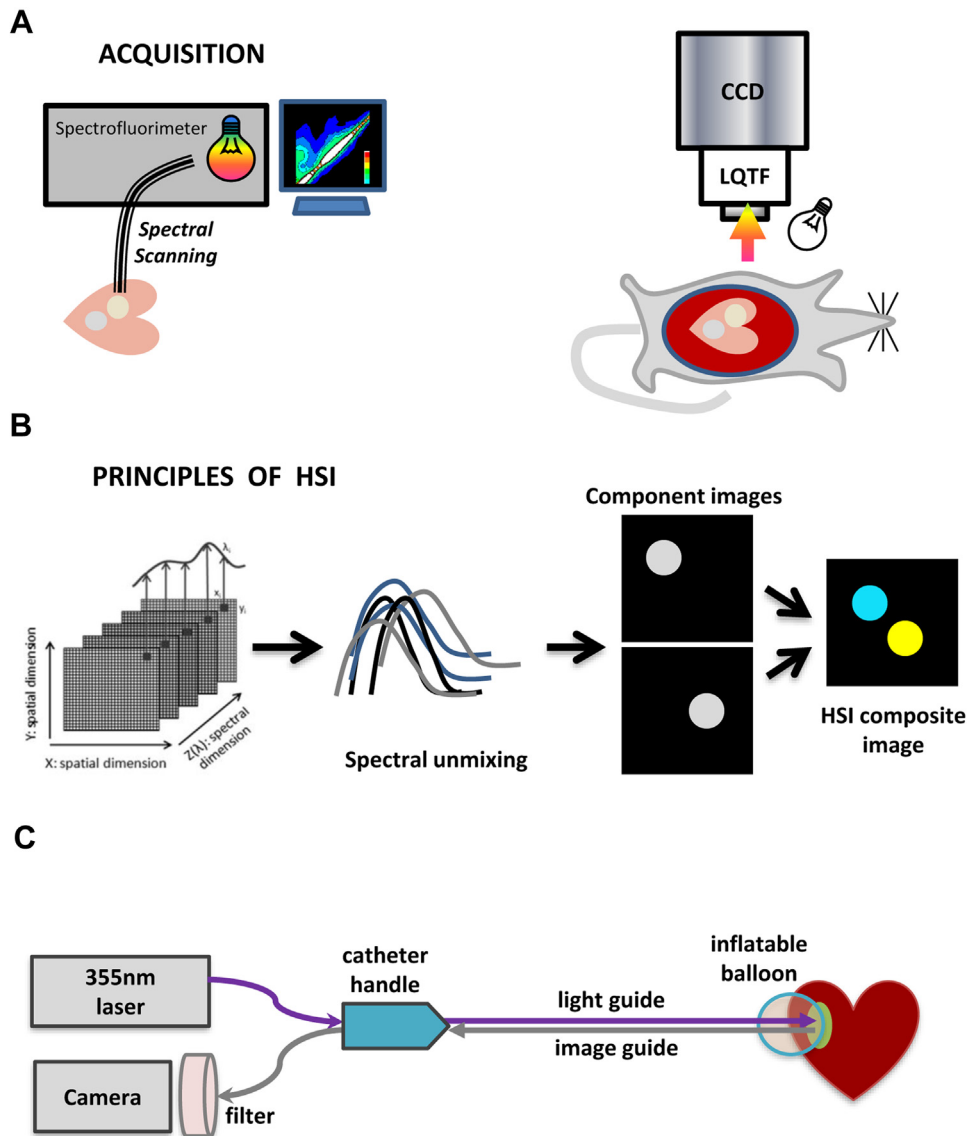
spatial resolution. The latter is the major limitation because viability gaps of <1 mm have been shown to conduct aberrant beats, leading to recurrent tachycardia and fibrillation.[3]

One way to achieve high spatial resolution imaging is via direct visual observation of the scarred tissue surface. With this goal in mind, several groups, including ours, have been developing percutaneous cardiac visualization catheters.[4–6] Availability of such catheters further suggests that more advanced methods of acquiring and analyzing the returning light can provide a wealth of additional information about the ventricular and atrial surfaces to be treated, with surfaces being endo- or epicardial. This was the main premise of our study. Specifically, we explored autofluorescence hyperspectral imaging (HSI) to help identify myocardial scar tissue and distinguish it from radiofrequency (RF) ablation sites. HSI spatial resolution highly depends on optical parts involved, but theoretically it can be 2–3 orders of magnitude more precise than the current cardiac imaging techniques.[7]

Figure 1   Cartoons of main protocols. **A:** Imaging setup for obtaining EEMs or hyperspectral images in blood-free and blood-perfused rat hearts. **B:** Principles involved in HSI spectral unmixing. **C:** Conceptual drawing of a percutaneous HSI catheter. CCD = charge coupled device; EEM = excitation-emission matrix; HSI = hyperspectral imaging; LQTF = liquid crystal tunable filter.

Methods

Animal surgery

Ablation procedures were performed in 2-month-old adult Sprague-Dawley rats (200–300 g) of mixed sexes. A thoracotomy was performed to expose the heart, followed by RF ablation on the epicardium of exposed ventricles. After the animals underwent 2 months of recovery, a second round of RF ablation was performed using the same anesthesia protocol. Alternatively, to create scar tissue by myocardial infarction, one of the left coronary artery branches was permanently ligated, followed by 2 months of animal recovery. On the final day of the protocol, the hearts were removed, perfused with saline, and used for either ex vivo HSI or spectral analysis. Alternatively, HSI of exposed heart surfaces was performed in live, blood-perfused animals (to avoid motion artifacts, the heart rate was lowered to 0.2 beats/sec by immersing

the animal into the ice bath). All studies conformed to the *Guide for the Care and Use of Laboratory Animals* and were approved by the Institutional Animal Use and Care Committee. Testing of the percutaneous HSI catheter in live pigs was conducted at a fully certified and accredited animal testing facility (Synchrony Labs, Durham, NC).

Excitation-emission matrix recordings

A dual fiber-optic guide connected to a spectrofluorometer (HORIBA Jobin Yvon FluoroMax-3, Edison, NJ) was placed at specified sites of the epicardial surface of the excised, saline-perfused rat ventricles (Figure 1A, left). The fiber has a 2 mm opening at the end, allowing it to deliver excitation light to the sample and collect emitted and reflected light back to the detector. To create an excitation-emission matrix (EEM), each site of interest was sequentially illuminated by the specified

wavelength while recording returning light spectra. Because of time involved in EEM acquisition, experiments were conducted in saline-perfused excised hearts to avoid running into contraction artifacts, blood coagulation, and animal loss.

HSI protocol

Hypercubes containing wavelengths ranging from 420 to 720 nm were collected using a Nuance FX HSI system (PerkinElmer/CRi, Waltham, MA) fitted with a Nikon AF Micro-Nikkor 60mm f/2.8D lens. A 4 × 3 cm field of view was captured at 1392 × 1040 pixels, yielding a 30 μm/pixel spatial resolution. The light emitting diode light source (either 365 nm or 4000 K warm white—both from Mightex, Pleasanton, CA) were oriented ~5–8 cm from the tissue surface (Figure 1A, right). A region of interest (ROI)–based selection, followed by the Nuance FX spectral unmixing algorithm, was used to extract lesion component images from each hypercube as described previously.[8,9] Placing ROIs at different random locations within the lesion did not significantly change the outcome of spectral unmixing (Supplemental Figure 1). Component images corresponding to scar, RF-ablated, or unablated tissue were then combined to form a pseudocolor HSI composite image (Figure 1B).

Percutaneous HSI catheter

A proof-of-concept version of the HSI catheter (Figure 1C) was put together using major elements of an autofluorescence imaging catheter previously reported in abstract form.[6,10,11] It encompasses a steerable handle, illumination, and imaging ports. A saline infusion port is used to inflate a urethane balloon for blood displacement. Image guide includes 17,000 individual 4-μm optical fibers and can be directly coupled to the Nuance FX HSI system.

Histopathology

Immediately after the experiment, hearts were Langendorff perfused with a Tyrode's solution containing 40 mM triphenyltetrazolium chloride (TTC) and then submerged in a TTC solution for an additional 15 minutes. To confirm the presence of collagen deposition at the ablation sites, the heart was fixed, sliced transmurally across the lesions, and stained with Masson's trichrome stain.

Statistical analysis

Values are presented as mean ± SD unless stated otherwise. One-way analysis of variance was performed on normalized fluorescence values for each wavelength. P values were determined using a Tukey post hoc test at 95% significance levels. The Pearson correlation coefficient was used to compare shapes of difference spectra.

Results
Visual appearance of RF lesions and scar tissue under broadband and UV illumination

When illuminated with white light within the open chest of a live animal, scar tissue and RF lesions appear as blanched,

pale regions of tissue (Figure 2A, left). When the same tissue was illuminated with UV light, RF lesions had a distinct yellow hue while scar tissue was nearly indistinguishable from unablated tissue (Figure 2A, middle). When the acquisition settings were changed to correspond to excitation and emission maxima of endogenous nicotinamide adenine dinucleotide (NADH) (365 nm/460 nm), RF lesions appeared as black holes (Figure 2A) because of the dramatic drop in NADH fluorescence as per previous findings by us and others.[12,13] Under 365 nm/460 nm excitation-emission settings, scar tissue exhibited a highly variable appearance, ranging from being intensely bright to being indistinguishable from surrounding muscle autofluorescence. Layers of the deposited collagen at scar sites were readily verified by Masson's trichrome staining in histology slides. Both scar and RF lesions were void of TTC staining when observed at the surface or when cross-sectioned (Figure 2B).

EEMs from RF ablation and scar sites

To better understand spectral ranges that can distinguish all 3 conditions, we acquired EEMs from the corresponding sites. Each EEM consists of hundreds of individual measurements at different excitation and emission wavelengths that are compiled into a 2-dimensional color map. The EEMs showed multiple spectral changes in the autofluorescence and reflectance profiles (Figure 3A). The major change was an expected drop in NADH-associated autofluorescence at RF ablation sites, which is represented by the disappearance of the NADH peak at ~350/465 nm (yellow arrow). The collagen deposited at scar sites appeared as a distinct new peak in the autofluorescence profile (red arrow). Its coordinates were different from those of the endogenous NADH fluorescence peak of viable muscle. The diffuse reflectance profile, represented by the diagonal line on EEMs, increased at the RF ablation and scar sites, confirming previous findings by us and others.[12,14]

Major spectral differences revealed by EEMs were confirmed and compared by acquiring profiles of emission intensity with 50 and 100 nm offsets from the excitation wavelength (Figure 3B). Most revealing was the quantitative outcome of spectral scanning using a 100 nm offset (Figure 3B, right). Traces from RF lesions (shown in green) reveal a dramatic loss of NADH fluorescence as compared to traces from unablated tissue (red). In contrast, the intensity of the collagen peak from scar tissue (blue) shows about equal intensity with the NADH peak collected from unablated tissue. This explains why autofluorescence from collagen deposition can compensate for the lack of the NADH signal in scar tissue, rendering it indistinguishable from the surrounding unablated tissue.

Choice of HSI modality

The spectral differences identified by EEMs suggested that 2 HSI modalities can help differentiate RF lesions from scar tissue. The first modality involves illumination with broadband white light while acquiring spectral images within the visible range. The second modality involves tissue illumination with
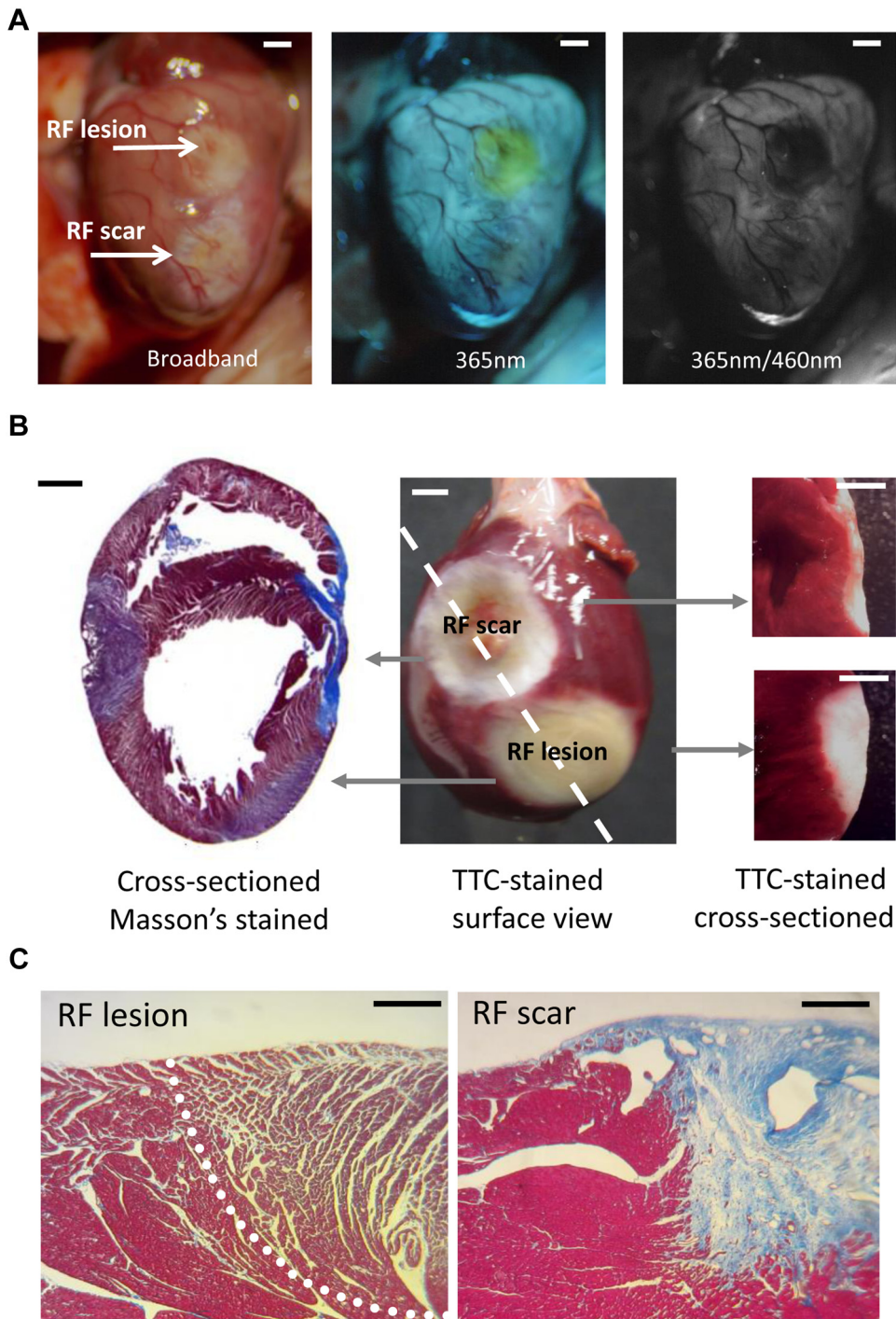
Figure 2   In vivo appearance of lesions and associated pathology. **A:** Appearance of a blood-perfused rat heart with an RF lesion and a scar from a previous ablation procedure under specified illumination/acquisition settings. Scale bars = 2 mm. **B:** Typical staining outcomes for a heart with an RF lesion and a scar from a previous RF ablation procedure. *Left:* Heart cross-section stained with Masson's trichrome stain. *Middle:* The appearance of both lesions on the ventricular surface after TTC staining. *Right:* Cross-sections showing the depth of both lesions. Scale bars = 2 mm. **C:** Histological appearance of an RF lesion (demarcated by a dashed line) and the scar site from a previous ablation procedure. Scale bars = 0.2 mm. RF = radiofrequency; TTC = triphenyltetrazolium chloride.

a UV source while collecting light across the visible range (Supplemental Figure 2). A side-by-side visual comparison of unmixing outcomes of the 2 modalities using 6 hearts suggested that the second modality (thereafter called autofluorescence HSI) provides better classification outcomes between the 3 tissue conditions. Figure 4 illustrates how it works: the raw traces extracted from different ROIs of the HSI hypercube have varied shapes and amplitudes. Yet when they are normalized, the spectra from pixels located within RF lesions (green traces) becomes distinct in shape from those located on unablated tissue (red traces) or scar sites (blue traces). To better illustrate these spectral divergences, the same data can be displayed as a difference plot between normalized intensity values vs that of unablated tissue. The
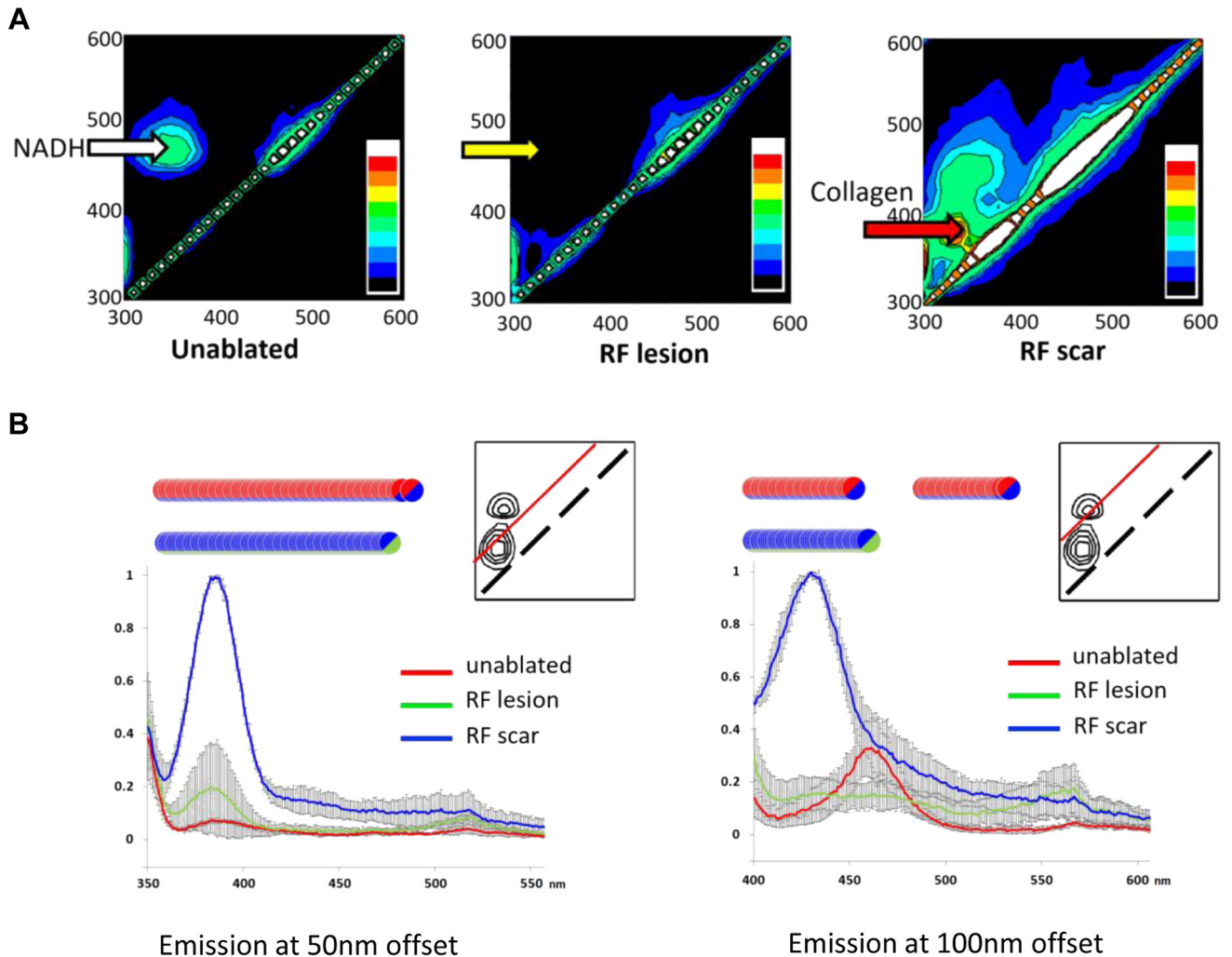
Figure 3 EEMs for unablated myocardium, RF lesion, and scar tissue. **A:** *Left:* EEM from healthy, unablated myocardium with a prominent NADH peak at 360/460 nm. *Middle:* EEM from an RF lesion demonstrating the loss of NADH and a moderate increase in diffuse reflectance (ie, intensity of the diagonal line). *Right:* EEM from the scar site showing the collagen fluorescence peak and a marked increase in diffuse reflectance. Shown EEM set is a representative of 4 independent experiments. The color bar depicts the relative intensity of the signal. **B:** Emission intensity profiles acquired with 50 and 100 nm offsets from the excitation wavelength (n = 3). The red line within the insets shows the location of such spectral profile within the EEM space. The insets also show the locations of collagen and NADH peaks (solid black lines). Circles indicate statistical difference between the 2 tissue states indicated by the corresponding color. EEM = excitation-emission matrix; RF = radiofrequency.

differences between normalized spectra from autofluorescence HSI hypercubes were significant across extended spectral ranges. Specifically, for pixels derived from scar areas, there is a significant increase in the 420–460 nm range that can be attributed to collagen deposition. For pixels derived from RF lesions, the intensity drops within a 420–500 nm range, indicating the loss of NADH, while the contribution from 560 to 650 nm wavelengths is significantly enhanced because of increased tissue scattering.

Effect of blood on observed spectral differences

Data shown in Figure 4 were obtained from excised, saline-perfused hearts. The next step was to confirm that similar spectral changes occur in vivo. This is shown in Figure 5, which illustrates the results of autofluorescence HSI done in the same heart as shown in Figure 4, but acquired while the heart was still within the chest of a live animal. When one compares

traces between Figure 4 and Figure 5, it becomes evident that the presence of blood in microcirculation has minimal impact on normalized autofluorescence spectra. In fact, an HSI hypercube of a blood-perfused heart can be successfully unmixed using spectral profiles derived from an HSI hypercube acquired from a saline-perfused heart or vice versa. Even more importantly, the observed changes were highly consistent between the animals; therefore, the spectral library from one animal heart could successfully unmix the HSI hypercube from another. Alternatively, spectra averaged from several hearts unmixed the HSI hypercube of a new heart without prior knowledge of the target tissue type (Figure 6A).

## HSI can distinguish other features within the field of view

Analysis of spectral information contained within the HSI hypercubes offers a wealth of additional features that can
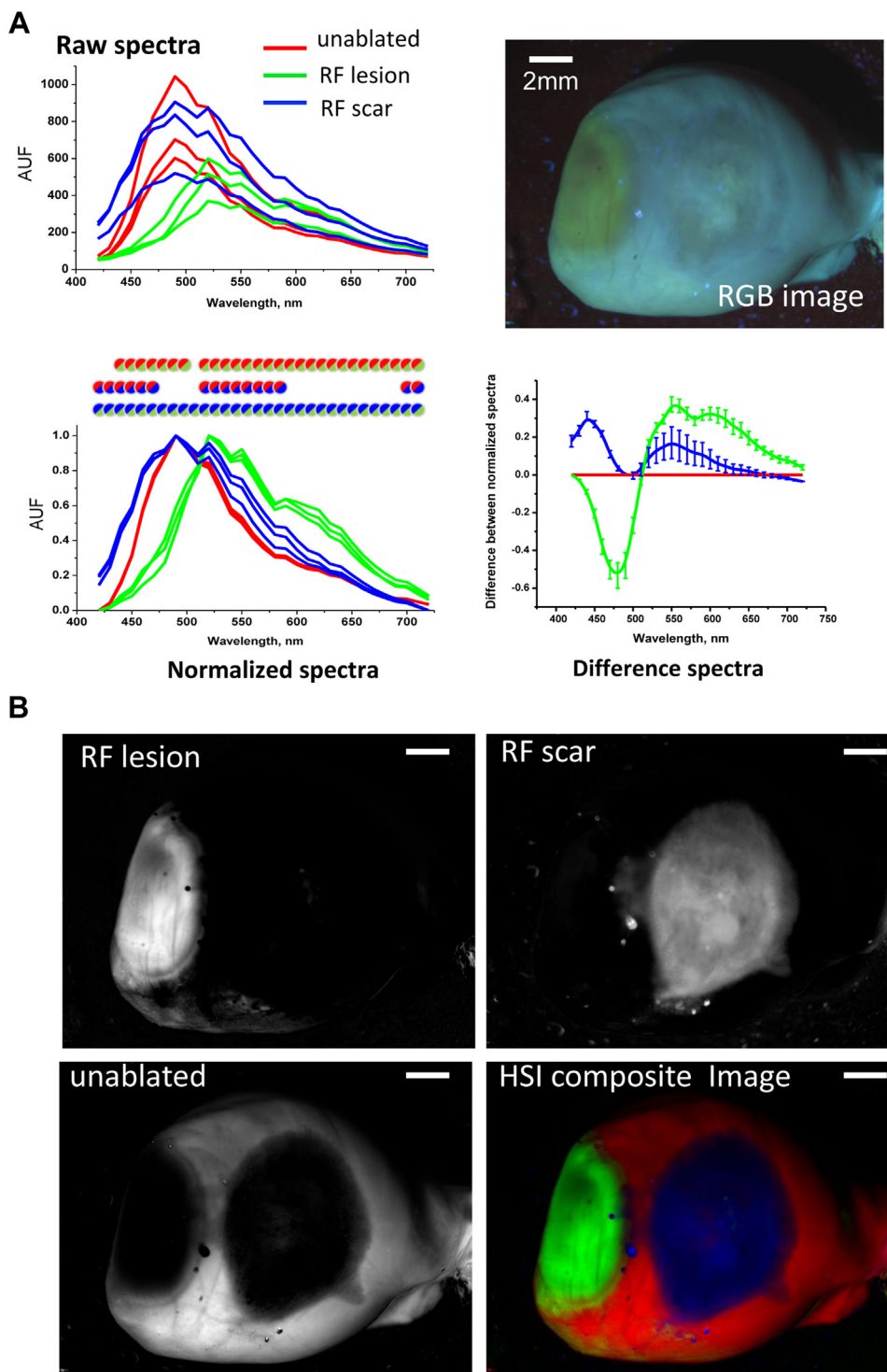
Figure 4   Spectral changes underlying autofluorescence HSI of saline-perfused hearts. **A:** *Top:* Raw spectral traces from 3 regions of interest within unablated, ablated, and scar areas of a saline-perfused, UV-illuminated heart. *Bottom:* The same spectra but normalized between their respective minima and maxima (circles indicate statistical difference between the 2 tissue states as per corresponding color). The average differences between the normalized spectra and those of unablated tissue are shown on the right. **B:** The 3 grayscale panels correspond to the HSI component images revealed by spectrally unmixing the HSI hypercube. The HSI composite image is shown using pseudocolor. Scale bars = 2 mm. AUF = arbitrary units of fluorescence; HSI = hyperspectral imaging; RF = radiofrequency; RGB = red green blue.

be clinically relevant. Figure 6B, for example, shows an image of the same heart as in Figure 6A, but with an additional ROI placed on blood vessels. By including additional target spectra in the unmixing algorithm, a highly vascularized scar boundary can be directly identified. In effect, visualization of any spectrally different targets within the field of view, whether endogenous (ie, fat deposits and conductive fibers) or exogenous (ie, sutures, patches, and guidewires), can be greatly enhanced by HSI.
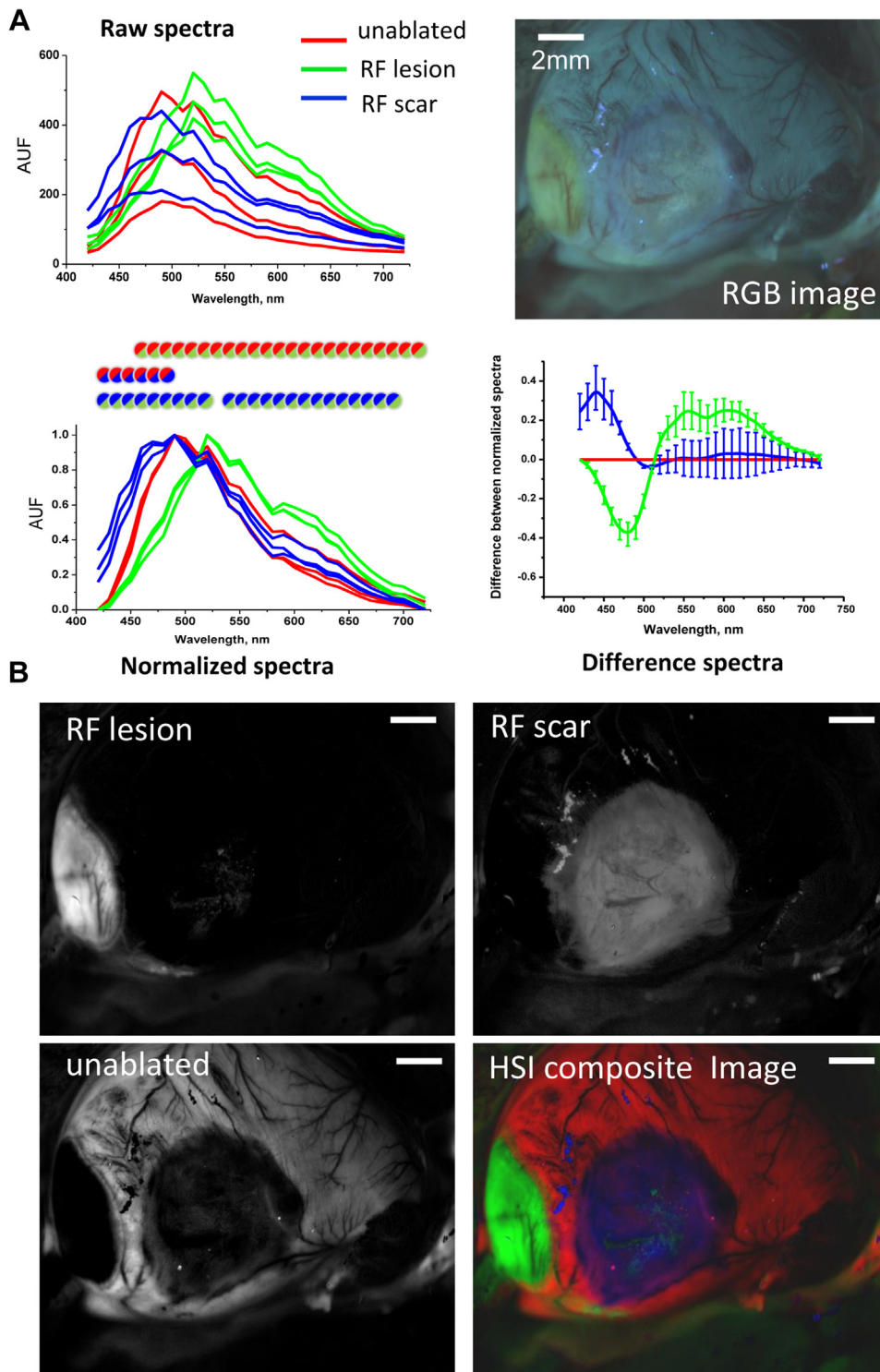
Figure 5 Spectral changes underlying autofluorescence HSI in blood-perfused hearts. **A:** *Top:* Raw and normalized spectral traces from 3 regions of interest within unablated, ablated, or scar areas of a blood-perfused, in vivo heart (circles indicate statistical difference between the 2 tissue states as per corresponding color). The HSI settings were identical to those used in the ex vivo experiment shown in Figure 4. *Bottom:* The quantitative differences between the normalized spectra for acute lesions, scar tissue, and unablated tissue. **B:** The 3 grayscale panels correspond to the HSI component images revealed by spectrally unmixing the HSI hypercube. The HSI composite image is shown using pseudocolor. Scale bars = 2 mm. AUF = arbitrary units of fluorescence; HSI = hyperspectral imaging; RF = radiofrequency; RGB = red green blue.
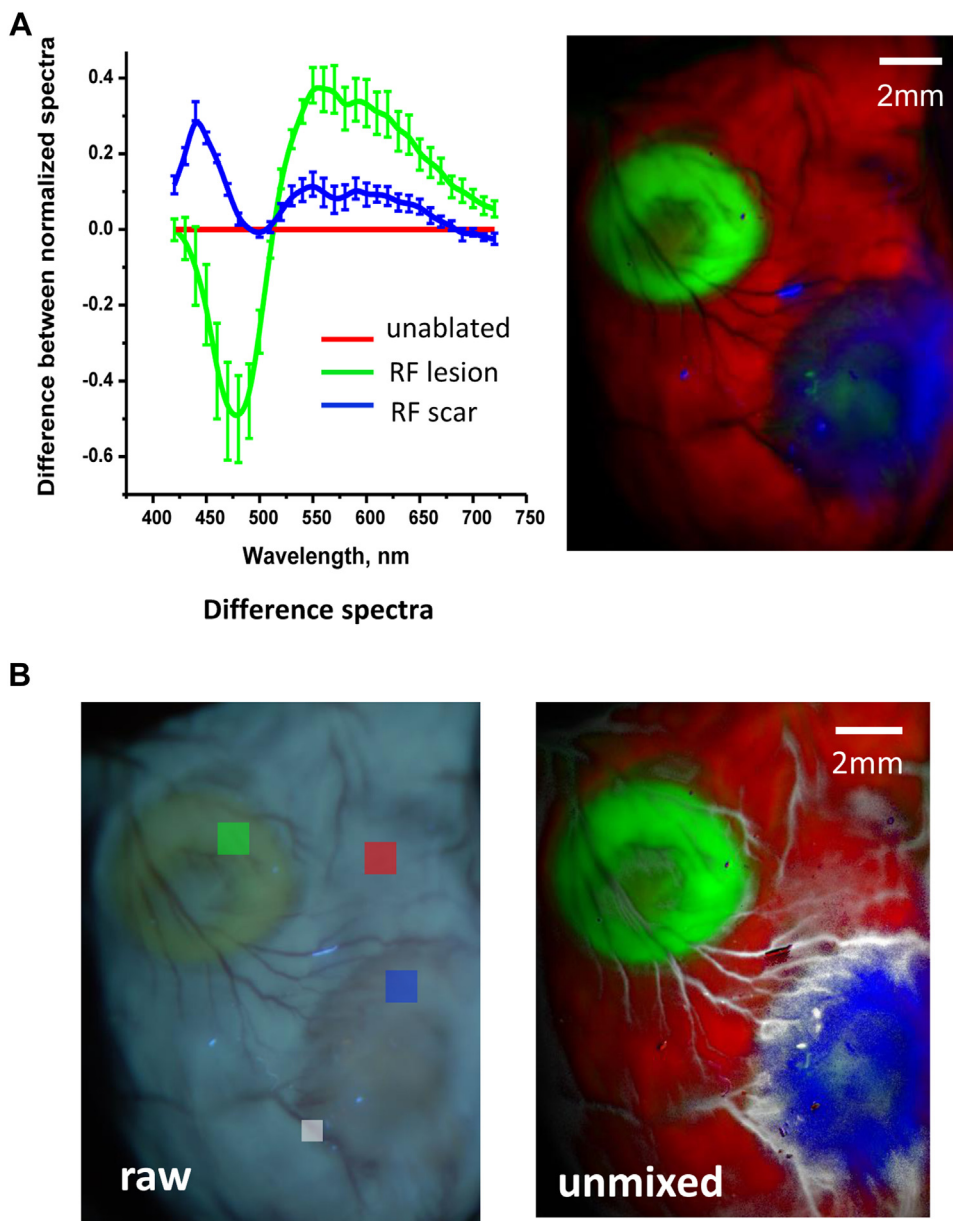
Figure 6   Use of spectral libraries and additional features that can be extracted from autofluorescence HSI data sets. **A:** Average spectral differences associated with RF lesions and scar tissue in blood-perfused hearts (n = 6). The HSI composite image shows the outcome of spectral unmixing when the mean spectra from the 6 hearts were used as a spectral library to unmix an HSI hypercube of another blood-perfused heart without prior knowledge of the target tissue type. **B:** An HSI hypercube contains information about other elements within the field of view that have unique spectral signatures. As an example, when an additional region of interest was placed on a blood vessel (small white box), the HSI unmixing algorithm used its spectral profile to reveal areas of extensive vascularization around the scar (shown in white pseudocolor). HSI = hyperspectral imaging; RF = radiofrequency.
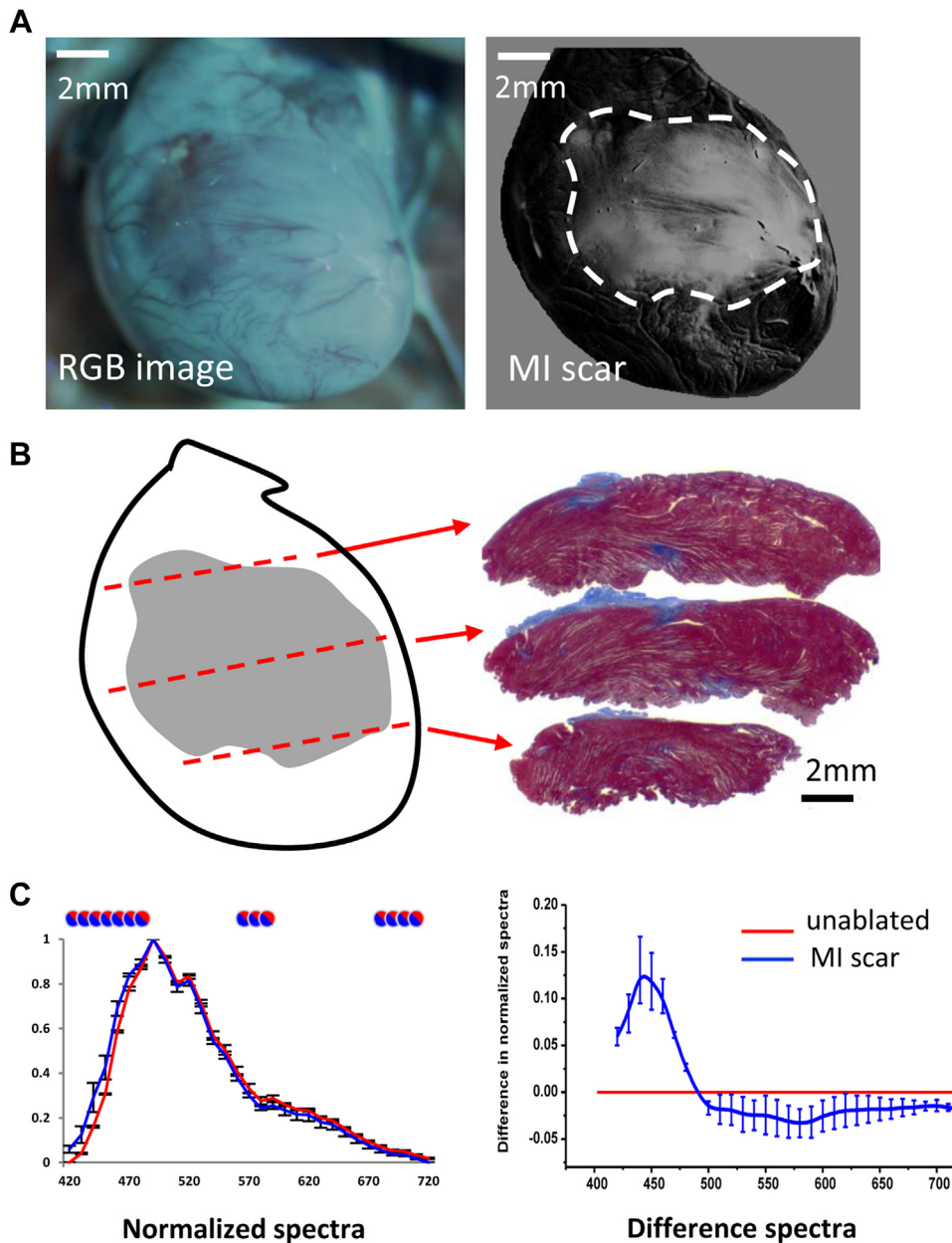
Identification of scar tissue from myocardial infarction and visualization of atrial RF lesions in vivo

Lastly, we confirmed that similar spectral changes occur in the cases of (1) myocardial infarction–induced ventricular scar and (2) RF lesions made on the endocardial surface of atrial tissue. The first set of these proof-of-principle experiments was done by imaging blood-perfused hearts of live rats, each with coronary ligation–induced ventricular scar (Figure 7). The use of autofluorescence HSI successfully outlined scar boundaries, with data being in good agreement with histology (Figure 7B). The observed spectral differences

were nearly identical to the ones we saw in hearts with scar tissue from healed RF ablation procedures (R = 0.96; P < .001) (blue difference curves in Figures 5A and 7C). Thus, scar regions in the infarcted animal group can be identified using spectra from RF-induced scar rats and vice versa.

The second set of confirmatory experiments was conducted in live pigs using a pilot version of a custom-made percutaneous HSI catheter (Figures 1C and 8A). Blood between the image guide and the atrial surface was displaced using a custom-made urethane balloon, followed by HSI acquisition. Spectral changes induced by RF ablation in blood-perfused pig atria exhibited high correlation with observed

Figure 7 Autofluorescence HSI for in vivo visualization of scar tissue from myocardial infarction. **A:** *Left:* An RGB image showing visual appearance of a scar on a left ventricular surface of a rat as it appears within the open chest of an animal under UV illumination. *Right:* HSI scar component image. **B:** *Left:* An outline of an HSI-identified scar with dotted lines used to section the heart. *Right:* Corresponding sections stained with Masson's blue. **C:** *Left:* Normalized spectra from control (red) and scar (blue) areas averaged from 3 animals. Circles indicate statistical difference between the 2 tissue states. *Right:* The average spectral difference between the normalized spectra of scar tissue and those of unablated tissue (red line). HSI = hyperspectral imaging; MI = myocardial infarction; RGB = red green blue.

changes in ablated ventricles of live rats ($R = 0.83$; $P < .001$) (green difference curves in Figures 5A and 8C) and were consistent with our previous reports on excised human and porcine atrial tissues.[9,15]

Discussion

The physiological assessment and visualization of myocardial scar tissue can be critically important for cardiac procedures such as the surgical treatment of ventricular and supraventricular arrhythmias.[1,16] The current noninvasive methods include different modalities of cardiac magnetic resonance imaging,[3,17] positron emission tomography,[1] and single photon emission computed tomography.[18] These methods are effective presurgery means to visualize the bulk of the scar within the myocardial wall. Yet they are poorly suitable for intraoperative surgical guidance, particularly when a direct high spatial resolution view of the cardiac surface is needed. Several minimally invasive, catheter-based methods are being developed to address this clinical need.
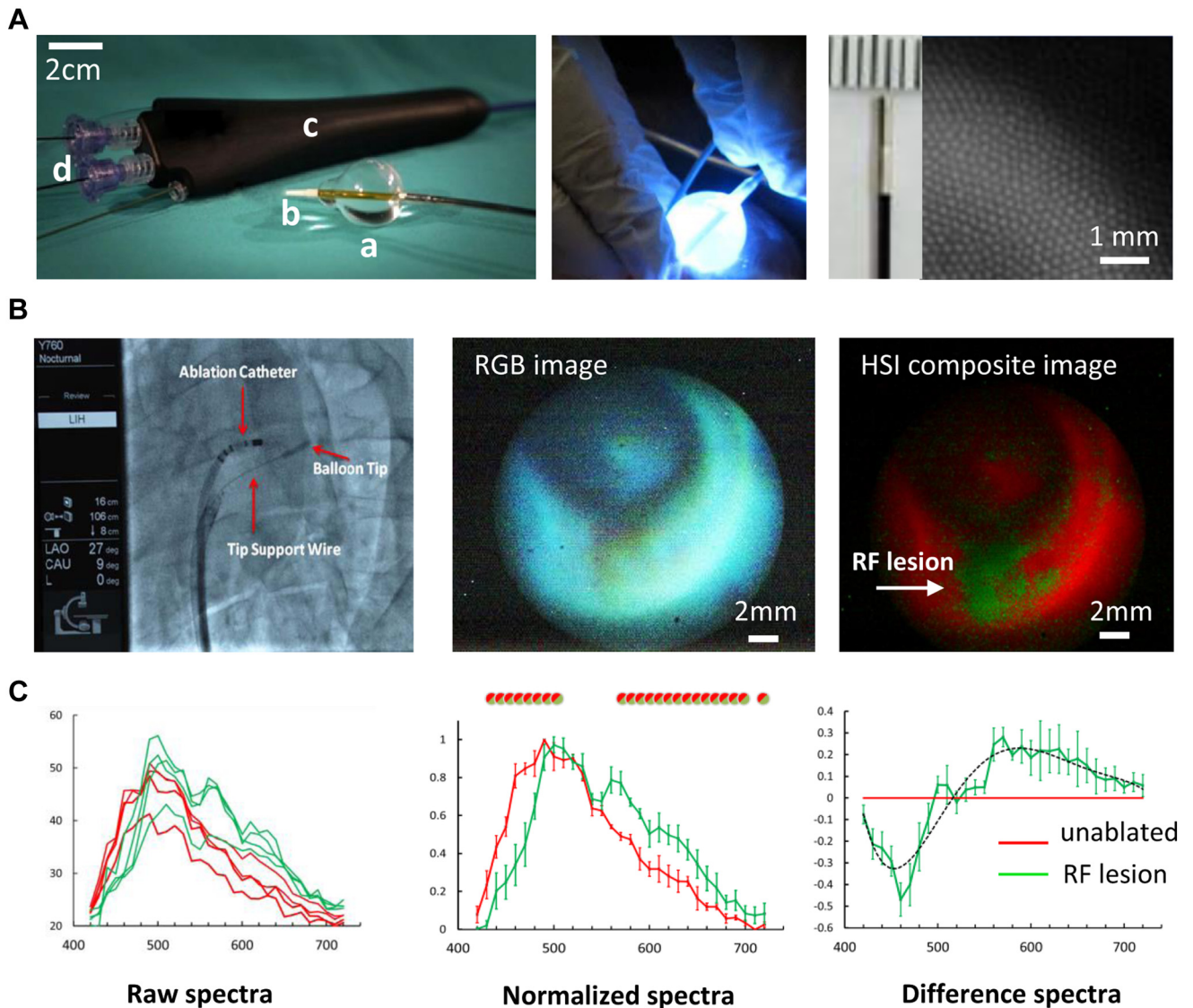
Figure 8   Proof-of-principle HSI visualization of endocardial RF lesions in live pigs. **A:** *Left:* Percutaneous HSI catheter composed of a custom-made urethane balloon (a), an atraumatic soft radiopaque tip (b), a catheter body (c), and a steerable handle. The catheter body includes several ports (d) allowing insertion of an illumination guide and an image guide and addition of saline for balloon inflation. *Middle:* Illumination guide delivers light from the 355 nm argon laser to the tip of the catheter. *Right:* Tip of the image guide and a closeup of an image produced by multiple 4-μm optical fibers. **B:** *Left:* Catheter can be deployed in the vasculature through a 12-F sheath placed in the femoral vein. *Right:* Composite hyperspectral image showing RF lesion in green and unablated tissue in red. **C:** Raw (*left*), normalized (*middle*), and difference (*right*) spectra from RF-ablated and intact porcine endocardial surfaces. Circles above normalized spectra indicate statistical difference between the 2 tissue states as per corresponding color. HSI = hyperspectral imaging; RF = radiofrequency; RGB = red green blue.

They include intracardiac echocardiography,[19] optical coherence tomography (OCT),[20,21] photoacoustic,[22] and polarization spectroscopy–based[23] catheters. The optical approach explored in this study presents another novel technique that can be implemented using percutaneous access.

HSI can be implemented with minimally invasive tools and without a need for contrast agents since it relies on intrinsic changes in tissue absorption, scattering, and endogenous fluorescence. The latter has proven to be a particularly reliable index because of a marked loss of muscle NADH at the ablation sites and the following buildup of the highly fluorescent collagen once the injured tissue heals.[24] Importantly, in addition to capturing changes in NADH or collagen

fluorescence (seen as a spectral drop and rise, respectively, within the 420–500 nm range), autofluorescence HSI detects changes in light scattering and absorption as these properties affect the travel path of emitted photons and the likelihood of their escape from the tissue.[9] Decreased tissue absorption therefore explains, for example, the increased contribution of longer wavelengths to the spectra of RF lesions (seen as a rise in normalized spectra at wavelengths above 530 nm).

Besides revealing the usefulness of autofluorescence HSI for scar identification, our experiments offered 2 noteworthy observations. The first was that reflectance HSI was less effective in distinguishing between RF lesions and scar tissue. The likely reason behind this was the relatively

nonselective increase in diffuse reflectance intensity across all visible wavelengths. In contrast, spectral changes in tissue autofluorescence profiles were much more distinct. The second important observation was that the presence of blood in microcirculation had a negligible effect on normalized autofluorescence profiles (compare normalized traces in Figure 4 vs Figure 5). This is because blood within vessels much larger than capillaries does not contribute significantly to the spectrum of returning light since virtually all visible light is absorbed during transit through large- and medium-sized vessels by red blood cells.[25] At the same time, the amount of red blood cells in capillary circulation does not exceed <1% of the total tissue volume,[25,26] so their spectral contribution is minimal.

The main limitation of autofluorescence HIS is its limited ability to sense lesion depth, as UV light does not penetrate into muscle for more than a millimeter.[27] Yet several studies have suggested that surface visualization of the scar can also be important. Specifically, the outcomes of ventricular tachycardia ablation procedures in patients with a history of post–myocardial infarction[28] or arrhythmogenic right ventricular dysplasia[29] were greatly improved by targeting the conducting channels within the scarred tissue near epi- or endocardial surfaces. Almost 60% of these conductive channels were found within the first millimeters of the ventricular wall.[17] This suggests that most of the arrhythmogenic substrate in patients with post–myocardial infarction can be approached with RF delivery near the endocardial surface. In such cases, the ability of HSI to distinguish viable tissue within the scar with submillimeter spatial resolution can be extremely useful.

High-resolution in vivo imaging of the scar surface can be useful to guide injections of stem cell–derived cardiomyocytes into the scar boundary.[30] Shown spectral differences can also be used for the design of smart injection needles with a fiber-optic sensor on the needle tip sensing surrounding tissue, including scar, blood vessel, or pool of injected dye–loaded cells.

Future clinical applications of HSI for noninvasive surgical guidance will require the manufacturing of specialized percutaneous visualization catheters or incorporation of HSI into the already existing cardiac visualization catheters.[4,5] Visual outcomes of a pilot version of the HSI catheter shown in Figure 8A can be significantly improved by gating hypercube acquisition to the R-R interval, optimizing optical ranges, and using more advanced unmixing algorithms.

Conclusion
Our data suggest that an autofluorescence-based, percutaneous HSI endoscope can be an excellent tool to reveal myocardial scar tissue in vivo. It can help reduce surgical time and improve the efficiency and effectiveness of several cardiac procedures. And since ablation procedures are commonly performed in other anatomical locations, the same principles can also be applied to many additional clinical targets for improved surgical guidance.

Appendix
Supplementary data
Supplementary data associated with this article can be found in the online version at https://doi.org/10.1016/j.hrthm.2017.12.014.

References
1. Rijnierse MT, Allaart CP, Knaapen P. Principles and techniques of imaging in identifying the substrate of ventricular arrhythmia. J Nucl Cardiol 2016; 23:218–234.
2. Andreu D, Ortiz-Pérez JT, Boussy T, Fernández-Armenta J, de Caralt TM, Perea RJ, Prat-González S, Mont L, Brugada J, Berruezo A. Usefulness of contrast-enhanced cardiac magnetic resonance in identifying the ventricular arrhythmia substrate and the approach needed for ablation. Eur Heart J 2014; 35:1316–1326.
3. Melby SJ, Lee AM, Zierer A, Kaiser SP, Livhits MJ, Boineau JP, Schuessler RB, Damiano RJ. Atrial fibrillation propagates through gaps in ablation lines: implications for ablative treatment of atrial fibrillation. Heart Rhythm 2008; 5:1296–1301.
4. Dukkipati SR, Cuoco F, Kutinsky I, Aryana A, Bahnson TD, Lakkireddy D, Woollett I, Issa ZF, Natale A, Reddy VY. Pulmonary vein isolation using the visually guided laser balloon. J Am Coll Cardiol 2015;66:1350–1360.
5. Sacher F, Derval N, Jadidi A, Scherr D, Hocini M, Haissaguerre M, Dos Santos P, Jais P. Comparison of ventricular radiofrequency lesions in sheep using standard irrigated tip catheter versus catheter ablation enabling direct visualization. J Cardiovasc Electrophysiol 2012;23:869–873.
6. Mercader M, Swift L, Jaimes R III, Armstrong K, Ransburry T, Amirana O, Sarvazyan N, Kay M. Real-time NADH fluorescence imaging catheter (Lux-Cath): a novel imaging system for evaluation of radiofrequency ablation lesions and gaps. Heart Rhythm 2013;5:A-9102.
7. Lin E, Alessio A. What are the basic concepts of temporal, contrast, and spatial resolution in cardiac CT? J Cardiovasc Comput Tomogr 2009;3:403–408.
8. Mansfield JR, Gossage KW, Hoyt CC, Levenson RM. Autofluorescence removal, multiplexing, and automated analysis methods for in-vivo fluorescence imaging. J Biomed Opt 2005;10:41207.
9. Gil DA, Swift LM, Asfour H, Muselimyan N, Mercader MA, Sarvazyan NA. Autofluorescence hyperspectral imaging of radiofrequency ablation lesions in porcine cardiac tissue. J Biophotonics 2017;10:1008–1017.
10. Koruth J, Kusa S, Dukkipati S, et al. Direct assessment of catheter-tissue contact and RF lesion formation: a novel approach using endogenous NADH fluorescence. Heart Rhythm 2015;5:S111.
11. Armstrong K, Ransbury T, Reddy VY, Koruth J, Amirana O, Mercader MA, Sarvazyan N, Larson C, Bowen J. Comparison of optical tissue interrogation vs impedance measurement for real-time monitoring of catheter-tissue contact and RF lesion progression. Heart Rhythm 2015;5:S117.
12. Swift L, Gil DAB, Jaimes R, Kay M, Mercader M, Sarvazyan N. Visualization of epicardial cryoablation lesions using endogenous tissue fluorescence. Circ Arrhythm Electrophysiol 2014;7:929–937.
13. Mercader M, Swift L, Sood S, Asfour H, Kay M, Sarvazyan N. Use of endogenous NADH fluorescence for real-time in situ visualization of epicardial radiofrequency ablation lesions and gaps. Am J Physiol Heart Circ Physiol 2012; 302:H2131–H2138.
14. Demos SG, Sharareh S. Real time assessment of RF cardiac tissue ablation with optical spectroscopy. Opt Express 2008;16:15286–15296.
15. Muselimyan N, Swift LM, Asfour H, Chahbazian T, Mazhari R, Mercader M, Sarvazyan N. Seeing the invisible: revealing atrial ablation lesions using hyperspectral imaging approach. PLoS One 2016;11:e0167760.
16. Aldhoon B, Kučera T, Smorodinová N, Martínek J, Melenovský V, Kautzner J. Associations between cardiac fibrosis and permanent atrial fibrillation in advanced heart failure. Physiol Res 2013;62:247–255.
17. Andreu D, Berruezo A, Ortiz-Pérez JT, Silva E, Mont L, Borràs R, de Caralt TM, Perea RJ, Fernández-Armenta J, Zeljko H, Brugada J. Integration of 3D

electroanatomic maps and magnetic resonance scar characterization into the navigation system to guide ventricular tachycardia ablation clinical perspective. Circ Arrhythmia Electrophysiol 2011;4:674–683.

18. Nazarian S, Beinart R. CMR-guided targeting of gaps after initial pulmonary vein isolation. JACC Cardiovasc Imaging 2014;7:664–666.

19. Bunch TJ, Weiss JP, Crandall BG, Day JD, Dimarco JP, Ferguson JD, Mason PK, McDaniel G, Osborn JS, Wiggins D, Mahapatra S. Image integration using intracardiac ultrasound and 3D reconstruction for scar mapping and ablation of ventricular tachycardia. J Cardiovasc Electrophysiol 2010;21:678–684.

20. Goergen CJ, Chen HH, Sakadžić S, Srinivasan VJ, Sosnovik DE. Microstructural characterization of myocardial infarction with optical coherence tractography and two-photon microscopy. Physiol Rep 2016;4:e12894.

21. Gan Y, Fleming CP. Extracting three-dimensional orientation and tractography of myofibers using optical coherence tomography. Biomed Opt Express 2013;4:2150.

22. Dana N, Di Biase L, Natale A, Emelianov S, Bouchard R. In vitro photoacoustic visualization of myocardial ablation lesions. Heart Rhythm 2013; 11:150–157.

23. Ahmad I, Gribble A, Ikram M, Pop M, Vitkin A. Polarimetric assessment of healthy and radiofrequency ablated porcine myocardial tissue. J Biophotonics 2016;9:750–759.

24. Prabhu SD, Frangogiannis NG. The biological basis for cardiac repair after myocardial infarction. Circ Res 2016;119:91–112.

25. Gandjbakhche AH, Bonner RF, Arai AE, Balaban RS. Visible-light photon migration through myocardium in vivo. Am J Physiol Heart Circ Physiol 1999; 277:H698–H704.

26. Silverman DA, Rakusan K. Red blood cell spacing in rat coronary capillaries during the cardiac cycle. Microvasc Res 1996;52:143–156.

27. Dana N, Asfour H, Emelianov S, Sarvazyan N. Surface illumination and autofluorescence modeling for assessment of radiofrequency ablation lesions. Circulation 2016;134:A18934.

28. Berruezo A, Fernandez-Armenta J, Andreu D, et al. Scar dechanneling: new method for scar-related left ventricular tachycardia substrate ablation. Circ Arrhythm Electrophysiol 2015;8:326–336.

29. Berruezo A, Fernandez-Armenta J, Mont L, Zeljko H, Andreu D, Herczku C, Boussy T, Tolosana JM, Arbelo E, Brugada J. Combined endocardial and epicardial catheter ablation in arrhythmogenic right ventricular dysplasia incorporating scar dechanneling technique. Circ Arrhythm Electrophysiol 2012;5:111–121.

30. Shiba Y, Fernandes S, Zhu W-Z, et al. Human ES-cell-derived cardiomyocytes electrically couple and suppress arrhythmias in injured hearts. Nature 2012; 489:332–335.